IEEE Access
Multidisciplinary | Rapid Review | Open Access Journal

Received January 11, 2022, accepted February 28, 2022, date of publication March 3, 2022, date of current version March 10, 2022.

Digital Object Identifier 10.1109/ACCESS.2022.3156694

Model Predictive Current Control With Online Parameter Estimation for Synchronous Reluctance Machine Controlled by High-Frequency Signal Injection Position-Sensorless

HYEON-SEONG KIM[1] AND KIBOK LEE[2], (Member, IEEE)
[1]Electrical Equipment Research and Development Team, Dawonsys Company Ltd., Ansan 15655, South Korea
[2]Department of Smart Mobility Engineering, Inha University, Incheon 22212, South Korea

Corresponding author: Kibok Lee (kibok.lee@inha.ac.kr)

This work was supported by the National Research Foundation of Korea (NRF) under Grant NRF-2021R1F1A1056095.

ABSTRACT Accurate machine parameters and rotor position information are essential in vector-controlled motor drive systems. However, machine parameter variations by various factors such as the current and the temperature degrade the performance of vector control. Also, a position sensor such as an encoder and a resolver increases the drive system cost. This paper proposes model predictive current control (MPCC) with the online parameter estimation for synchronous reluctance machines controlled by a high-frequency signal injection position-sensorless method. This approach removes the need for accurate knowledge about the system and eliminates the need for the position sensor. The proposed method adopts a recursive least-square (RLS) to estimate the electrical machine parameters in real-time. The estimated parameters are used for the deadbeat continuous control set (CCS) MPCC and the position-sensorless control. The high-frequency signal injection method is modified to be suitable for the proposed CCS-MPCC method, ensuring stable operation in the low-speed regions. Simulation and experimental results are provided to verify the performance of the proposed control method.

INDEX TERMS Model predictive current control (MPCC), recursive-least square (RLS), high-frequency signal injection, position-sensorless, synchronous reluctance machines (SynRM).

I. INTRODUCTION

In electric machine drives, the model predictive current control (MPCC) has been applied to various machines such as induction machine (IM) [1], permanent magnet synchronous machine (PMSM) [2], switched reluctance machine (SRM) [3], and synchronous reluctance machine (SynRM) [4]. Although model predictive control (MPC) suffers from intensive computation in real-time, MPC provides high dynamic responses, easy implementation, and a simple control structure [5]. Also, the development of advanced digital microprocessors makes the MPC getting attention in many applications. However, parameter dependency is still a drawback of the MPCC. The machine parameters such as resistance, inductance, and permanent magnet flux are easily varied by the temperature, the current magnitude, and so on [6], [7]. The control performance is affected by variations of machine parameters used to calculate the voltage command or to predict the future stator current.

Various studies to reduce the parameter dependency of the MPCC have been conducted [8]–[11]. In [8], the model-free predictive current control (MFPCC) based on the finite control set (FCS) method is introduced. This method does not require any machine parameter information and only utilizes the measured stator current and the current variations by applied voltage vector stored in look-up tables (LUTs). The method in [9] proposes the FCS-MPCC using a recursive least-square (RLS) self-commissioning model. The RLS

The associate editor coordinating the review of this manuscript and approving it for publication was Ramani Kannan.

algorithm adapts the machine parameters used to predict the future currents. The sensitivity of the machine parameter variations is reduced. The FCS-MPCC method in [10] proposes using the predicted slopes of current vectors to select the optimal voltage vectors. This method does not require the motor parameter information and LUTs. However, the FCS methods in [8]–[10] inherently have current ripple issues because only one among eight voltage vectors that can be generated by a voltage source inverter (VSI) is applied in a switching period. Also, the switching frequency is varied by the applied voltage vector patterns [5]. The method in [11] proposed the ultra-local model based MFPCC, which adopts the deadbeat continuous control set (CCS) method. This method can apply any desired voltage vectors in a switching period, resulting in improved dynamics compared to FCS-MPCC and the fixed switching frequency. The methods introduced in [8]–[11] can reduce the parameter dependency of MPCC. However, these methods require position sensors, such as resolver or encoder, which increase system cost, size, and reliability issues [12]–[15].

Various strategies were proposed to eliminate the position sensor in the MPCC [16]–[20]. In [16] and [17], the rotor position information is extracted from the back-electromotive force (back-EMF) and the stator current ripples, respectively. Similarly, the method in [18] uses the current variation by the applied dual-voltage vectors to estimate the rotor position. However, the approaches in [16]–[18] are the model-based sensorless method. Thus, the estimation performance is easily degraded by the parameter variations. In [19], the modified finite position algorithm based on the model reference adaptive system (MRAS) was proposed for SynRM drives. This method is relatively robust to the parameter variations. But the stator resistance is still required, which results in the position estimation error, particularly in the low-speed region. The method in [20] proposes the CCS-MPCC without the estimated rotor position for the surface-mounted PMSM (SPMSM). However, this method estimates the back-EMF using machine parameters. Therefore, this method is suitable for the medium and high-speed regions, and the I-F scalar control is adopted in the low-speed region.

In [21], we have proposed a deadbeat MPCC with online parameter estimation for SynRM drives controlled by high-frequency signal injection-based sensorless vector control. This method estimates the machine parameter online and adopts the sensorless method to eliminate the need for the position sensor. In this work, we provide a more detailed review of the state-of-the-art and discuss the implementation of the proposed method in detail. The RLS algorithm for the online machine parameter estimation and the high frequency signal injection sensorless are introduced in section II. In section III, the deadbeat CCS-MPCC applicable to the high frequency signal injection based sensorless method is proposed. This MPCC based sensorless control allows stable operation in low-speed regions, including zero-speed. Simulation and experimental results are provided to validate the performance of the proposed method in sections IV and V.

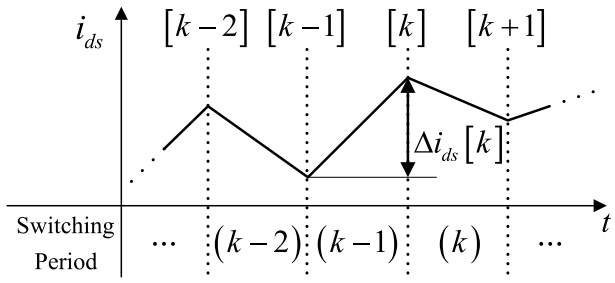

FIGURE 1. Stator current change by applied voltages in switching periods.

II. RLS PARAMETER ESTIMATOR WITH A CONVENTIONAL HIGH-FREQUENCY SIGNAL INJECTION POSITION-SENSORLESS

In this section, the RLS estimator and the conventional high-frequency signal injection position-sensorless method are briefly introduced. The parameter estimation performance of the RLS estimator in the drive system controlled by the high-frequency signal injection sensorless method is analyzed.

A. RLS ALGORITHM FOR PARAMETER ESTIMATION

As well known, dq-axis voltage equations of the SynRM in the rotor reference frame are expressed as:

$$\begin{aligned} v_{ds} &= R_s i_{ds} + L_{ds}\frac{di_{ds}}{dt} - \omega_r \lambda_{qs} \\ v_{qs} &= R_s i_{qs} + L_{qs}\frac{di_{qs}}{dt} + \omega_r \lambda_{ds} \end{aligned} \tag{1}$$

where v_{ds}, v_{qs} are the dq-axis voltages, i_{ds}, i_{qs} are the dq-axis currents, R_s is the stator resistance, L_{ds}, L_{qs} are the dq-axis stator inductances, λ_{ds}, λ_{qs} are the dq-axis stator flux linkages, and ω_r is the rotor electrical speed.

Fig. 1 shows the d-axis current by applied d-axis voltages. The round bracket and the square bracket represent the switching period and the sampling number, respectively. The d-axis current variation during one switching period Δi_{ds} calculated at the $[k]$th sampling time is a result of the d-axis voltage applied during the $(k-1)$th switching period. The d-axis voltage in (1) is expressed in the discrete form using the Backward-Euler method as:

$$\begin{aligned} v_{ds}(k-1) = R_s[k]\, i_{ds}[k] + L_{ds}[k]\frac{\Delta i_{ds}[k]}{T_s} \\ -\omega_r[k]\,\lambda_{qs}[k] \end{aligned} \tag{2}$$

$$\Delta i_{ds}[k] = i_{ds}[k] - i_{ds}[k-1] \tag{3}$$

where T_s means a controller sampling time. The d-axis current derivative (referred as output) can be rewritten as:

$$\underbrace{\frac{\Delta i_{ds}[k]}{T_s}}_{\text{Output}} = \underbrace{(v_{ds}(k-1))}_{\text{Known}} \underbrace{\left(\frac{1}{L_{ds}[k]}\right)}_{\text{Unknown}}$$

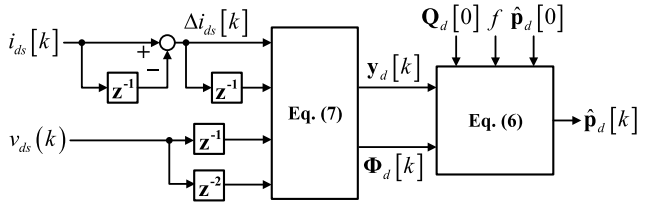

FIGURE 2. RLS estimator to estimate the unknown parameters [9].

$$+\underbrace{(1)}_{\text{Known}}\underbrace{\left(\frac{\omega_r[k]\,\lambda_{qs}[k]-R_s[k]\,i_{ds}[k]}{L_{ds}[k]}\right)}_{\text{Unknown}}$$
$$=\underbrace{\phi_{d1}[k]}_{\text{Input}}\underbrace{p_{d1}[k]}_{\text{Parameter}}+\underbrace{\phi_{d2}[k]}_{\text{Input}}\underbrace{p_{d2}[k]}_{\text{Parameter}} \tag{4}$$

where ϕ_{d1}, ϕ_{d2} are the d-axis inputs, and p_{d1}, p_{d2} are the d-axis parameters. Each term on the right side is the product of the known value (referred as input) and the unknown value (referred as parameter). Eq. (4) can be simply expressed as the inner vector product as:

$$\begin{aligned}\frac{\Delta i_{ds}[k]}{T_s}&=\begin{bmatrix}\phi_{d1}[k] & \phi_{d2}[k]\end{bmatrix}\begin{bmatrix}p_{d1}[k] & p_{d2}[k]\end{bmatrix}^{\mathrm{T}}\\&=\phi_d^v[k]\cdot\mathbf{p}_d[k]\end{aligned} \tag{5}$$

where ϕ_d^v is the d-axis input vector and $\mathbf{p}_d$ is the d-axis parameter vector.

This study adopts the RLS algorithm for estimating parameters that is one of the most widespread methods [9]. Two unknown values (parameters) in (4) can be estimated by the below RLS estimator [9].

$$\begin{aligned}\mathbf{G}_d[k]&=\mathbf{Q}_d[k-1]\,\mathbf{\Phi}_d^{\mathrm{T}}[k]\\&\quad\times\left\{\mathbf{\Phi}_d[k]\,\mathbf{Q}_d[k-1]\,\mathbf{\Phi}_d^{\mathrm{T}}[k]+f\mathbf{I}\right\}^{-1}\\\hat{\mathbf{p}}_d[k]&=\hat{\mathbf{p}}_d[k-1]+\mathbf{G}_d[k]\left\{\mathbf{y}_d[k]-\mathbf{\Phi}_d[k]\,\hat{\mathbf{p}}_d[k-1]\right\}\\\mathbf{Q}_d[k]&=\frac{1}{f}\left\{\mathbf{Q}_d[k-1]-\mathbf{G}_d[k]\,\mathbf{\Phi}_d[k]\,\mathbf{Q}_d[k-1]\right\}\end{aligned} \tag{6}$$

The hat "^" indicates the estimated values. $\hat{\mathbf{p}}_d[k]=\begin{bmatrix}\hat{\mathbf{p}}_{d1}[k] & \hat{\mathbf{p}}_{d2}[k]\end{bmatrix}^{\mathrm{T}}$ is the estimated d-axis parameter vector, $\mathbf{y}_d[k]=\begin{bmatrix}\Delta i_{ds}[k]/T_s & \Delta i_{ds}[k-1]/T_s\end{bmatrix}^{\mathrm{T}}$ is the d-axis output vector, $\mathbf{\Phi}_d[k]=\begin{bmatrix}\phi_d^v[k]\,;\,\phi_d^v[k-1]\end{bmatrix}$ is the d-axis regressors matrix, $\mathbf{G}_d[k]$ is the d-axis 2×2 gain matrix, $\mathbf{Q}_d[k]$ is the d-axis 2×2 estimation error covariance matrix, $\mathbf{I}$ is a 2×2 unit matrix, and f is a forgetting factor. The forgetting factor f is a control factor that determines the weight between the measured and estimated values.

Fig. 2 shows the block diagram of the RLS estimator for the parameter estimation. The output vector and the regressors matrix are determined by the input voltage and the measured current as:

$$\begin{aligned}\mathbf{\Phi}_d[k]&=\begin{bmatrix}\phi_d^v[k]\,;\quad\phi_d^v[k-1]\end{bmatrix}\\\mathbf{y}_d[k]&=\begin{bmatrix}\Delta i_{ds}[k]/T_s & \Delta i_{ds}[k-1]/T_s\end{bmatrix}^{\mathrm{T}}\end{aligned} \tag{7}$$

The initial value of the parameter vector $\hat{\mathbf{p}}_d[0]$ and the estimation error covariance matrix $\mathbf{Q}_d[0]$ are required, which are generally determined by experiments [9], [15]. In this work, the initial values of first parameters $\hat{\mathbf{p}}_{d1}[0]$ are set to 1, the second parameters $\hat{\mathbf{p}}_{d2}[0]$ are set to zero, and the estimation error covariance matrix $\mathbf{Q}_d[0]$ are set to 2×2 unit matrix, experimentally.

With this RLS estimator, the parameters $\hat{\mathbf{p}}_d$ used in the MPCC can be estimated. Also, the q-axis parameters can be estimated with the same process. Next, the performance of the RLS for the machine controlled by the conventional high-frequency signal injection sensorless method is analyzed.

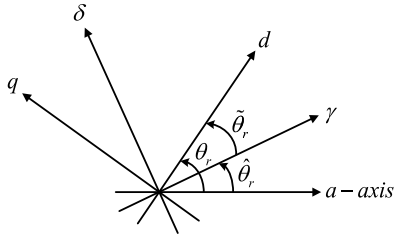

FIGURE 3. The real and the estimated coordinate.

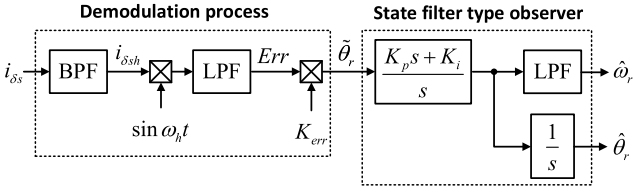

FIGURE 4. State filter type observer and the demodulation process for rotor speed and position estimation.

B. RLS ESTIMATOR WITH A CONVENTIONAL HIGH-FREQUENCY SINUSOIDAL VOLTAGE SIGNAL INJECTION METHOD [12]

If the injected high-frequency is sufficiently faster than the electrical rotor speed, the resistance voltage drops and the back-EMF terms in (1) can be neglected. Considering only high-frequency components, the high-frequency impedances can be obtained as:

$$z_{dsh}\approx\frac{v_{dsh}}{i_{dsh}}=\omega_h L_{dsh};\qquad z_{qsh}\approx\frac{v_{qsh}}{i_{qsh}}=\omega_h L_{qsh} \tag{8}$$

where ω_h is the injected high-frequency, L_{dsh}, L_{qsh} are the dq-axis stator inductances at the injected high-frequency, z_{dsh}, z_{qsh} are the dq-axis high-frequency impedances, v_{dsh}, v_{qsh} and i_{dsh}, i_{qsh} are the dq-axis high-frequency components of voltages and currents, respectively.

To obtain the position error information, the high-frequency voltage is injected only in the estimated γ-axis.

$$v_{\gamma sh}^*=V_{\gamma h}\cos\omega_h t;\qquad v_{\delta sh}^*=0 \tag{9}$$

where the superscript "*" indicates the command and $V_{\gamma h}$ is the amplitude of the high-frequency sinusoidal voltage injected in the estimated γ-axis. The relationship between the real dq-axis and the estimated $\gamma\delta$-axis is described in Fig. 3.

When the high-frequency sinusoidal voltage is injected in the γ-axis, the high-frequency component of the δ-axis

current can be obtained as:

$$i_{\delta sh} = \frac{V_{\gamma h} \cos \omega_h t}{z_{dsh} z_{qsh}} \left(-\frac{1}{2} z_{diff} \sin 2\tilde{\theta}_r \right) \tag{10}$$

where $\tilde{\theta}_r$ is the rotor position estimation error between the real rotor position θ_r and the estimated rotor position $\hat{\theta}_r$, and z_{diff} is the difference of dq-axis high-frequency impedances.

In (10), the high-frequency component of the δ-axis current includes the information of the rotor position estimation error. Assumed that the estimation error $\tilde{\theta}_r$ is sufficiently small, the input error Err can be obtained by a demodulation process in Fig. 4 as:

$$Err \approx \frac{V_{\gamma h} \left(L_{qsh} - L_{dsh} \right)}{2\omega_h L_{dsh} L_{qsh}} \tilde{\theta}_r = \frac{\tilde{\theta}_r}{K_{err}} \tag{11}$$

where K_{err} is determined by stator inductance which is varied by the operating condition.

In Fig. 4, $i_{\delta s}$ is the δ-axis stator current, the BPF is a band-pass filter, the LPF is a low-pass filter, and K_p and $K_{\rm i}$ denote the proportional and integral gain, respectively, of the observer. The electrical rotor speed and position are estimated with the demodulation process and the state filter type observer. In this sensorless method, the cross-coupling inductance can cause a small position estimation error [22]–[24]. But this work ignored the cross-coupling inductance for the sake of simplification.

In (4), the RLS estimator output is set to the derivative of the current. Therefore, the estimation of the $\gamma\delta$-axis parameters $\hat{\mathbf{p}}_{\gamma\delta}$ can be failed if the current change in one switching period is too small. The γ-axis current has sufficient difference during one switching period by the high-frequency sinusoidal voltage injected in the γ-axis. However, the δ-axis current change is too small in the steady-state, so the RLS estimator can be failed to estimate the parameters.

Fig. 5 shows the simulation results for an RLS estimator with a conventional high-frequency signal injection in the γ-axis. The SynRM parameters are listed in Table 1. The γ-axis parameter $p_{\gamma 1}$ is estimated well due to the injected high-frequency signal. On the other hand, the δ-axis parameter $p_{\delta 1}$ maintains the initial value due to no current variation in the δ-axis, and the parameter estimation is failed. Therefore, an additional signal is required to estimate δ-axis parameters.

III. PROPOSED DEADBEAT MPCC BASED ON HIGH-FREQUENCY SIGNAL INJECTION POSITION-SENSORLESS CONTROL

A. PROPOSED SQUARE-PULSE CURRENT INJECTION IN THE δ-AXIS

The proposed method additionally injects the high-frequency square-pulse current in the δ-axis for estimating δ-axis parameters by the RLS estimator.

$$i^*_{\delta sp}[k] = I^*_{\delta p} \Pi[k]$$
$$\Pi[k] = \begin{cases} +1, & k = 1, 3, 5, \cdots \\ -1, & k = 2, 4, 6, \cdots \end{cases} \tag{12}$$

TABLE 1. Test SynRM nominal parameters.

Parameter	Unit	Symbol	Values
Rated Power	[kW]	P_e	5.5
Rated Speed	[r/min]	n_r	1500
Rated Torque	[Nm]	T_e	18
Rated Voltage (line-line)	[V]	V_s	220
Rated Phase Current	[Arms]	i_s	13.4
Pole	-	n	4
Stator Resistance	[Ω]	R_s	0.19
Stator d-axis Inductance	[mH]	L_{ds}	28.5
Stator q-axis Inductance	[mH]	L_{qs}	12
Inertia	[Nm/rad·s^{-2}]	J	0.1
PWM Switching Period	[μsec]	T_s	100

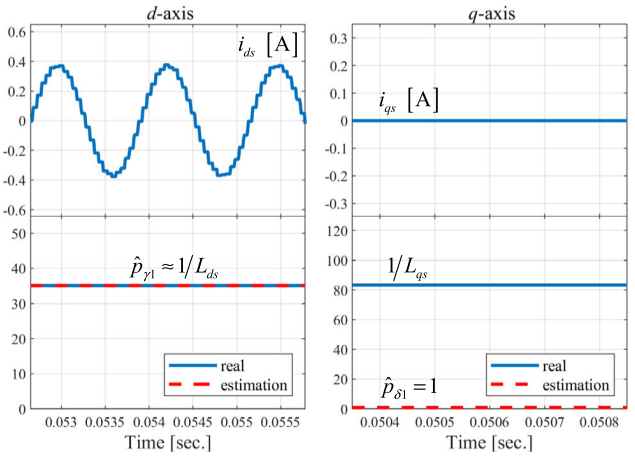

FIGURE 5. Simulation results of the RLS estimator with a conventional high-frequency signal injection in the γ-axis.

The subscript "p" indicates the square-pulse component, Π is the square-pulse function, and $I^*_{\delta p}$ is the amplitude of the injected δ-axis square-pulse current command. In this study, the frequency of the q-axis injected pulse is set to half of the switching frequency. On the other hand, the frequency of d-axis sinusoidal voltage is set to 800 Hz. If the signal having a similar or same frequency is injected in the q-axis, the q-axis current in (10) for the sensorless control is affected, which may cause the failure of the sensorless control. To minimize interference, the frequency of the q-axis pulse current is set to be much faster than that of the d-axis sinusoidal voltage.

The δ-axis current consists of a main component $i_{\delta sm}$, the square-pulse component $i_{\delta sp}$, and the high-frequency component $i_{\delta sh}$ caused by the high-frequency sinusoidal voltage injected in γ-axis.

$$i_{\delta s} = i_{\delta sm} + i_{\delta sp} + i_{\delta sh}$$
$$i_{\delta sc} \equiv i_{\delta s} - i_{\delta sh} \tag{13}$$

where the command component of the δ-axis current $i_{\delta sc}$ is defined as the current components except for the current component caused by the γ-axis high-frequency sinusoidal voltage.

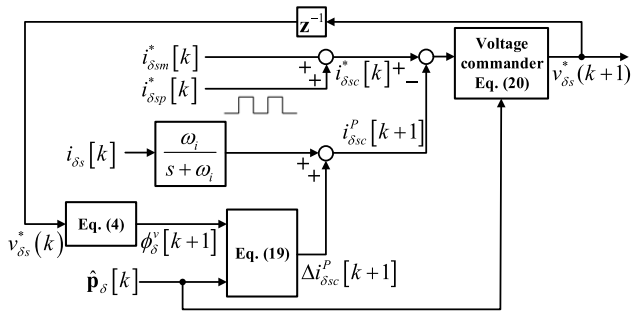

FIGURE 6. Block diagram of the proposed deadbeat MPCC (δ-axis).

B. PROPOSED DEADBEAT MPCC

This section presents the proposed deadbeat MPCC for the voltage command calculation considering the injected high-frequency signals.

In the estimated coordinate, $[k]$th δ-axis current can be obtained from (3) and (4) as:

$$i_{\delta s}[k] = i_{\delta s}[k-1] + T_s v_{\delta s}(k-1)\, p_{\delta 1}[k] + T_s p_{\delta 2}[k] \quad (14)$$

where $v_{\delta s}$, $i_{\delta s}$ are the δ-axis stator voltage and current, and $p_{\delta 1}$, $p_{\delta 2}$ are the δ-axis first and second parameter, respectively.

Most predictive control methods suffer from the delay by the controller calculation time. The general solution is that the controller calculates a voltage command one switching period earlier [25]. In the proposed method, the $(k+1)$th voltage command is also calculated in the (k)th switching period.

Substituting $k+2$ to k in (14), the $(k+1)$th δ-axis voltage can be obtained as:

$$v_{\delta s}(k+1) = \frac{i_{\delta s}[k+2] - i_{\delta s}[k+1] - T_s p_{\delta 2}[k+2]}{T_s p_{\delta 1}[k+2]} \quad (15)$$

The voltage command to generate the command current component defined in (13) is rewritten as:

$$v^*_{\delta s}(k+1) = \frac{i_{\delta sc}[k+2] - i_{\delta sc}[k+1] - T_s p_{\delta 2}[k+2]}{T_s p_{\delta 1}[k+2]} \quad (16)$$

Actually, the RLS estimator acts as a time-varying low-pass filter [26]. The forgetting factor in the RLS estimator is similar to the time constant of the low-pass filter. If the forgetting factor is sufficiently large, the RLS estimator attenuates the high-frequency component $\hat{\mathbf{p}}_{\delta h}$ and estimates the low-frequency component $\hat{\mathbf{p}}_{\delta l}$. With this in mind, assuming the estimated parameters are almost constant during two switching periods, the $[k+1]$ and $[k+2]$th estimated parameters are set to the $[k]$th values.

$$v^*_{\delta s}(k+1) = \frac{i_{\delta sc}[k+2] - i_{\delta sc}[k+1] - T_s \hat{p}_{\delta 2l}[k]}{T_s \hat{p}_{\delta 1}[k]} \quad (17)$$

In (17), the δ-axis $[k+1]$th current $i_{\delta sc}[k+1]$ can be predicted by adding the predicted $[k+1]$th current variation $\Delta i^P_{\delta sc}[k+1]$ to the $[k]$th current $i_{\delta sc}[k]$. The current $i_{\delta sc}[k]$ can be obtained from the sampled current $i_{\delta s}[k]$. A low-pass filter is adopted to remove the high-frequency components in the sampled current as follows.

$$i^P_{\delta sc}[k+1] = \frac{\omega_i}{D+\omega_i} i_{\delta s}[k] + \Delta i^P_{\delta sc}[k+1] \quad (18)$$

The superscript "P" indicates the predicted values, ω_i is an angular cutoff frequency of the low-pass filter, and D means the differential operator.

During the (k)th switching period, the δ-axis $[k+1]$th current variation $\Delta i^P_{\delta sc}[k+1]$ can be predicted by substituting $k+1$ to k in (5) as follows.

$$\Delta i^P_{\delta sc}[k+1] = T_s\left(\phi^v_\delta[k+1] \cdot \hat{\mathbf{p}}_\delta[k]\right) \quad (19)$$

In (19), the $[k+1]$th input vector $\phi^v_\delta[k+1] = \begin{bmatrix} v_{\delta s}(k) & 1 \end{bmatrix}$ is a known value during the (k)th switching period, and the $[k]$th estimated parameters are used to predict the command component of the δ-axis $[k+1]$th current variation.

Finally, assuming the current command is almost constant during two switching periods, the $[k+2]$th current in (17) is set as the $[k]$th current command. The δ-axis voltage command is expressed as:

$$v^*_{\delta s}(k+1) = \frac{i^*_{\delta sc}[k] - i^P_{\delta sc}[k+1] - T_s \hat{p}_{\delta 2l}[k]}{T_s \hat{p}_{\delta 1}[k]} \quad (20)$$

Fig. 6 shows the block diagram of the proposed deadbeat MPCC to calculate the δ-axis voltage command.

Next, the δ-axis current by the square-pulse current command is analyzed. The δ-axis current generated by the applied voltage is obtained by substituting (20) into (14) as:

$$\begin{aligned} i_{\delta s}[k] &\approx i^*_{\delta sc}[k-2] + \underbrace{i_{\delta sh}[k-1] + T_s p_{\delta 2h}[k]}_{\text{high-frequency component}} \\ &+ \underbrace{\frac{-\omega_i}{D+\omega_i} i_{\delta sh}[k-2]}_{\text{filtered high-frequency component}} + \underbrace{\frac{D}{D+\omega_i} i_{\delta sc}[k-2]}_{\text{controller error}} \end{aligned} \quad (21)$$

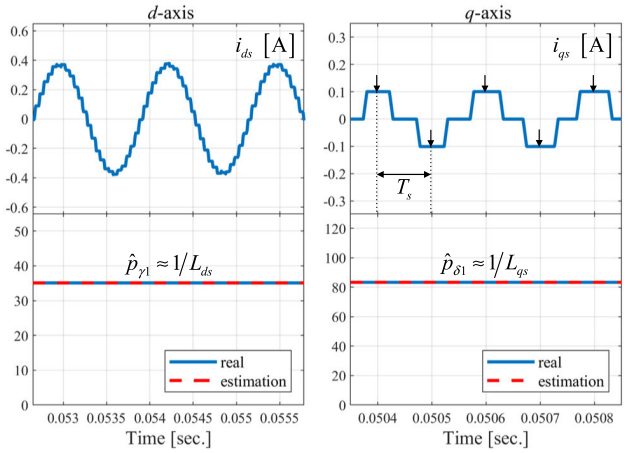

FIGURE 7. Simulation results of the RLS estimator with the proposed δ-axis square-pulse current injection.

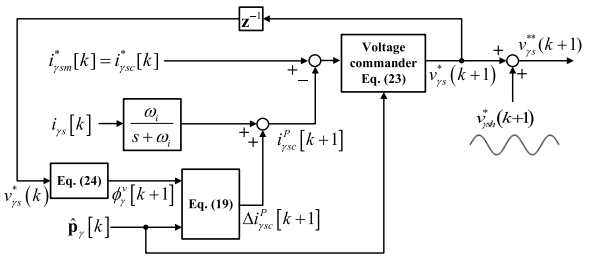

FIGURE 8. Block diagram of the proposed deadbeat MPCC (γ-axis).

The detailed equation expansion is described in Appendix. In (21), the actual current tracks the current command with two sampling periods delay and contains the high-frequency components.

Fig. 7 shows the simulation results for an RLS estimator with the proposed square-pulse current injection method. The high-frequency sinusoidal voltage is injected in the γ-axis, and the high-frequency square-pulse current is injected in the δ-axis. The downward arrows represent the controller sampling instance, where the current is measured. The simulation results show that the δ-axis first parameter $p_{\delta 1}$ is estimated well, unlike the case with only the sinusoidal voltage injection shown in Fig. 5. Notably, although the square-pulse is commanded, the resulted current has the trapezoidal form due to the voltage pulses applied by the SVPWM based VSI.

Next, the γ-axis voltage command is calculated. As previously mentioned in section II, the high-frequency sinusoidal voltage is injected in the γ-axis to estimate the rotor position and speed. Fig. 8 shows the block diagram to calculate the γ-axis voltage command in the proposed deadbeat MPCC. The command voltage generated by the MPCC is added with the injected high-frequency sinusoidal voltage.

$$v^{**}_{\gamma s} = v^*_{\gamma s} + v^*_{\gamma sh} \tag{22}$$

Similar to the δ-axis voltage in (16), the γ-axis voltage command is calculated as:

$$v^*_{\gamma s}(k+1) = \frac{i^*_{\gamma sc}[k] - i^P_{\gamma sc}[k+1] - T_s \hat{p}_{\gamma 2l}[k]}{T_s \hat{p}_{\gamma 1}[k]} \tag{23}$$

This voltage command $v^*_{\gamma s}$ is used as the input vector ϕ^v_γ to predict the low frequency component of the current variation $\Delta i^P_{\gamma sc}$ as follows.

$$\phi^v_\gamma[k+1] = \begin{bmatrix} v^*_{\gamma s}(k) & 1 \end{bmatrix} \tag{24}$$

Similar to the derivation of the δ-axis current in (21), the γ-axis current generated by the applied voltage is derived as:

$$\begin{aligned} i_{\gamma s}[k] &\approx i^*_{\gamma sc}[k-2] \\ &+ \underbrace{i_{\gamma sh}[k-1] + T_s\left(p_{\gamma 2h}[k] + v^*_{\gamma sh}(k-1)\, p_{\gamma 1}[k]\right)}_{\text{high-frequency component}} \\ &+ \underbrace{\frac{-\omega_i}{D+\omega_i} i_{\gamma sh}[k-2]}_{\text{filtered high-frequency component}} + \underbrace{\frac{D}{D+\omega_i} i_{\gamma sc}[k-2]}_{\text{controller error}} \end{aligned} \tag{25}$$

In (25), the actual current tracks the current command with two sampling periods delay and includes the high-frequency components.

The injected δ-axis square-pulse current can cause any effect in position-sensorless control in Fig. 4. However, if the frequency of the square-pulse current is significantly faster than that of the injected sinusoidal voltage, the effect of the injected square-pulse current in the demodulation process is negligible.

Fig. 9 shows a block diagram of the proposed control scheme, which consists of the RLS estimator, the speed and the current controller, and the high-frequency position-sensorless control. The rotor speed is controlled by the conventional proportional integral (PI) controller.

IV. SIMULATION RESULTS

Simulation tests were conducted to validate the performance of the proposed method. The machine parameters are listed in Table 1. The amplitude and the frequency of the injected high-frequency γ-axis voltage are set to 50 V and 800 Hz. The amplitude of the injected δ-axis current is set to 0.1 A and 5 kHz, so the δ-axis voltage to make the high-frequency square-pulse current has 24 V amplitude at the nominal parameters. The forgetting factor is set to $f = 0.99$. The bandwidth of the observer and the speed controller in Fig. 4 is set to 5 Hz and 2 Hz, respectively. The proposed method injects the high frequency sinusoidal and pulse signals for the sensorless control and the parameter estimation, which causes the torque and speed ripples. To minimize the response of the speed controller to the speed ripple, the bandwidth of the speed controller and the observer is set to low values.

Fig. 10 shows the simulation results of the proposed method. Initially, the $\gamma\delta$-axis current commands set to zero. The high-frequency sinusoidal voltage and the square-pulse current are injected. The rotor position and speed, the machine parameters, and $\hat{K}_{err}$ are estimated at the initialization time. The γ-axis current increases to 50% of the rated current to make the stator flux, and the rotor speed increases to 1,200 [r/min]. The error of the rotor position estimation $\tilde{\theta}_r$ is small in all speed regions.

In the simulation, the stator inductance is estimated by the RLS estimator, and the K_{err} is calculated as:

$$\hat{K}_{err}[k] = \frac{2\omega_h}{V_{\gamma h}\frac{\omega_L}{s+\omega_L}\left(\hat{p}_{\gamma 1}[k] - \hat{p}_{\delta 1}[k]\right)} \tag{26}$$

where ω_L is the cutoff angular frequency of the low-pass filter. The low-pass filter is used to remove the ripple components in

the estimated stator inductance. The K_{err} in Fig. 4 is updated to maintain the constant bandwidth of the speed observer in the position-sensorless control. The cutoff angular frequency of the low-pass filter for the estimated parameters is set to 5 rad/s, and the $\hat{K}_{err}$ is initially set to -1.

Fig. 11 shows the simulation results for the estimation of the stator inductance and $\hat{K}_{err}$ when the dq-axis stator

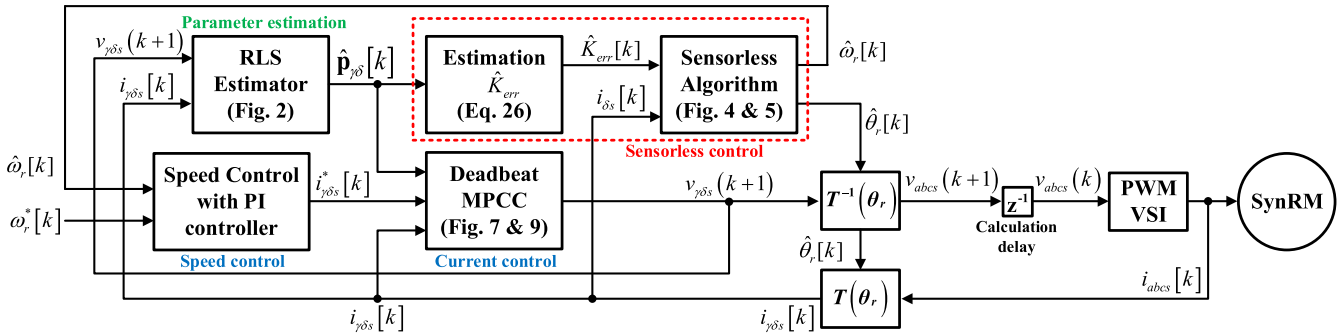

FIGURE 9. Block diagram of the proposed control scheme.

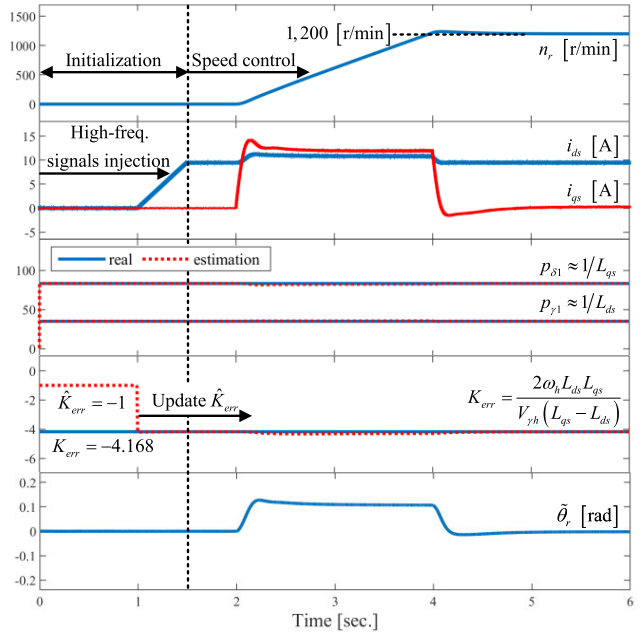

FIGURE 10. Simulation results of the proposed method.

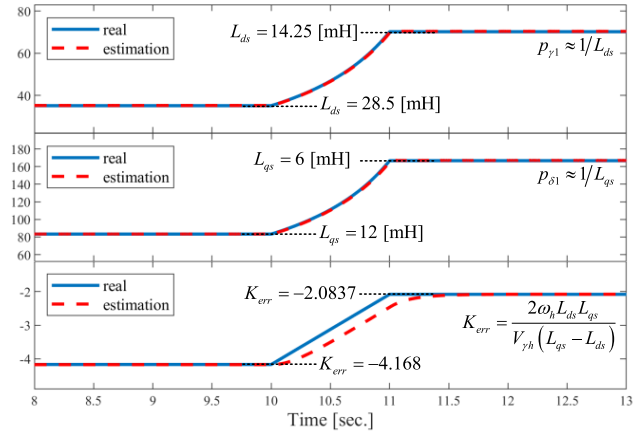

FIGURE 11. Simulation results: estimation of stator inductance and $\hat{K}_{err}$ when the stator inductances are varied (1,200 [r/min] and no-load conditions).

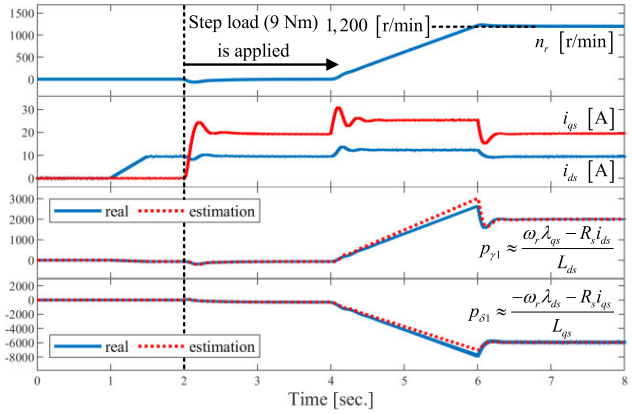

FIGURE 12. Simulation results: parameters $\hat{p}_{\gamma\delta 2}$ estimation when the speed and dq-axis currents are varied.

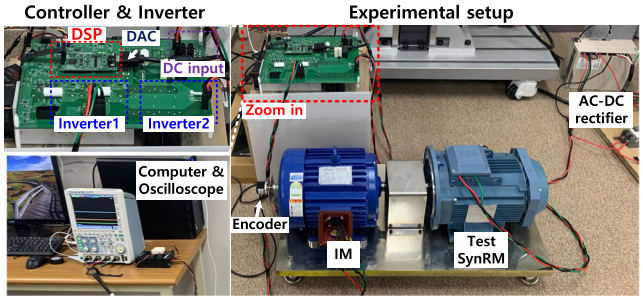

FIGURE 13. Experimental setup of the SynRM drive system.

inductances are varied at a fixed rotor speed of 1,200 [r/min] under no load condition. From $t = 10$ to 11 [sec.], the dq-axis stator inductances are intentionally reduced by half of the nominal parameters. The stator inductance estimated by the RLS estimator tracks well the actual inductance. Also, the estimated $\hat{K}_{err}$ tracks the correct value although the delay by the low-pass filter exists.

Fig. 12 shows the estimation of the parameters $\hat{p}_{\gamma\delta 2}$ under different speed and load conditions. At $t = 2$ [sec.], the step load of 9 [Nm] is applied at zero-speed. From $t = 4$ to 6 [sec.], the speed increases to 1,200 [r/min]. In the whole operating conditions, the estimated second parameters $\hat{p}_{\gamma\delta 2}$ track well the actual values.

V. EXPERIMENTAL RESULTS

Experimental tests were conducted with a 5.5kW SynRM to validate the performance of the proposed method. In Fig. 13, the experimental setup consists of the tested SynRM and an

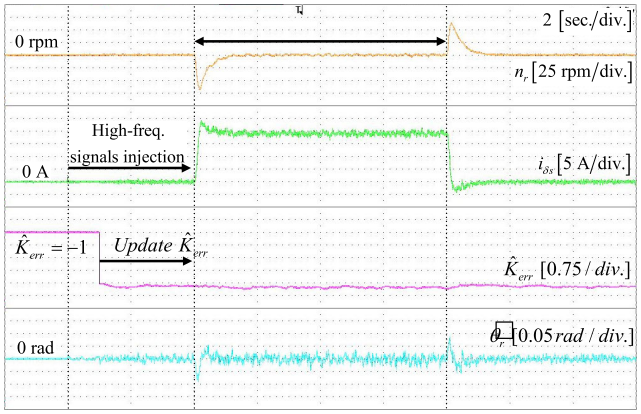

FIGURE 14. Experimental results of the proposed position-sensorless method at zero-speed condition. Rotor speed (orange line), δ-axis current (green line), estimated $\hat{K}_{err}$ (purple line), and position error (cyan line).

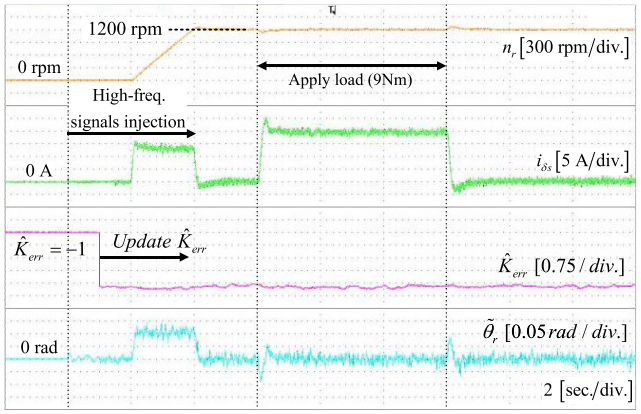

FIGURE 15. Experimental results: speed control responses of the proposed position-sensorless method. Rotor speed (orange line), δ-axis current (green line), estimated $\hat{K}_{err}$ (purple line), and position error (cyan line).

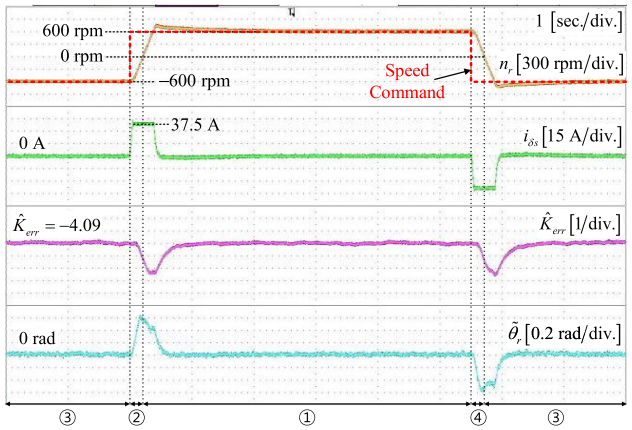

FIGURE 16. Experimental results: four-quadrant operation of the proposed position-sensorless method. Rotor speed (orange line), δ-axis current (green line), estimated $\hat{K}_{err}$ (purple line), and position error (cyan line).

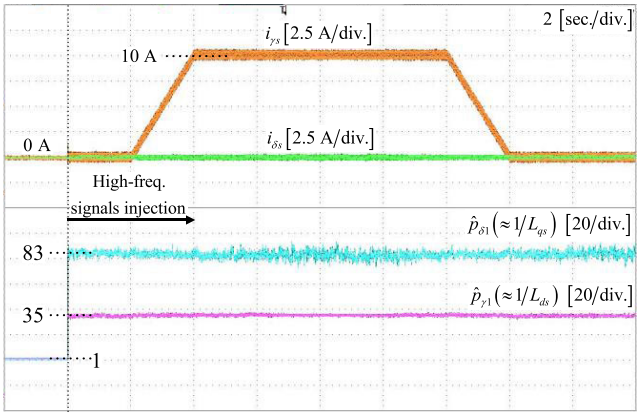

FIGURE 17. Experimental results: first parameters $\hat{p}_{\gamma\delta 1}$ estimation of the proposed method at zero speed: γ-axis current (orange line), δ-axis current (green line), and estimated $\gamma\delta$-axis first parameters by the RLS estimator. $\hat{p}_{\gamma 1}$ (purple line) and $\hat{p}_{\delta 1}$ (cyan line).

IM as a load motor. The SynRM nominal parameters are given in Table 1. The digital signal processor (TMS-320F28346) embedded VSI is used to drive the test and load motors. An encoder sensor is used to monitor the actual rotor position so as to validate the proposed method.

Fig. 14 shows the step load test results of the proposed method at zero-speed condition. A step load of 9 [Nm] is applied from $t = 6$ to 14 [sec.]. The estimated $\hat{K}_{err}$ is matched with the actual value of –4.168, even in the step load condition. The maximum position error at the instant of the step load change is about –0.1 [rad.].

Fig. 15 shows the speed control performance of the proposed high-frequency signal injection position-sensorless method. From $t = 4$ to 6 [sec.], the rotor speed increases to 1,200 [r/min], which is over the medium speed. The rated speed of the tested motor is 1,500 [r/min]. A step load of 9 [Nm] is applied from $t = 8$ to 14 [sec.]. The rotor speed n_r and the δ-axis current $i_{\delta s}$ show good performances. Also, the $\hat{K}_{err}$ is estimated well. The position error $\tilde{\theta}_r$ is sufficiently small in all operating ranges, and the maximum position error at the step load is about –0.1 [rad.].

Fig. 16 shows the four-quadrant operation of the proposed method. The numbers below the figure denote the corresponding quadrant. Initially, the rotor speed is –600 [r/min] in steady state. The step-type 600 [r/min] speed command is applied from $t = 2$ to 7.5 [sec.]. The estimated $\hat{K}_{err}$ tracks the actual value of –4.168 with the delay by the LPF. The maximum position error $\tilde{\theta}_r$ is about –0.6 [rad.] during the transient condition.

Fig. 17 shows the estimated $\gamma\delta$-axis first parameters $\hat{p}_{\gamma\delta 1}$ by the RLS estimator while the γ-axis stator current is varied under the zero-speed condition. The δ-axis current command is set to zero while injecting the δ-axis square-pulse. Before the high-frequency signals are injected, the estimated $\gamma\delta$-axis first parameters $\hat{p}_{\gamma\delta 1}$ are set to the initial value 1. From $t = 2$ [sec.], the parameters are estimated by the RLS estimator. The γ-axis current increases to 10 [A] from $t = 4$ to 6 [sec.], and decreases to 0 [A] from $t = 14$ to 16 [sec.]. The estimated $\gamma\delta$-axis first parameter $\hat{p}_{\gamma 1}$ ($\approx 1/L_{ds}$) and $\hat{p}_{\delta 1}$ ($\approx 1/L_{qs}$) are matched well with the actual parameters ($p_{\gamma 1} = 35.09$ and $p_{\delta 1} = 83.33$) even if the stator current is varied.

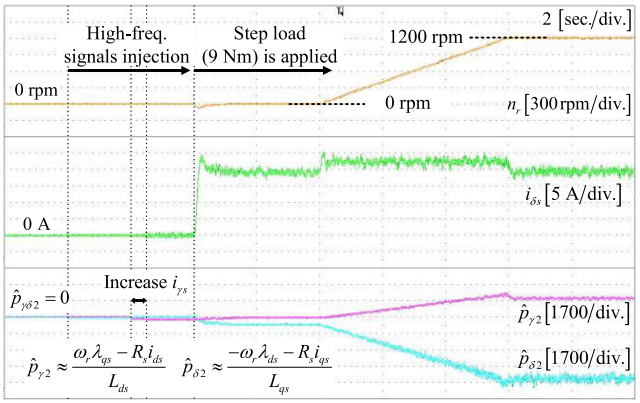

FIGURE 18. Experimental results: second parameters $\hat{p}_{\gamma\delta 2}$ estimation of proposed method: rotor speed (orange line), δ-axis current (green line), and estimated $\gamma\delta$-axis second parameters by the RLS estimator. $\hat{p}_{\gamma 2}$ (purple line) and $\hat{p}_{\delta 2}$ (cyan line).

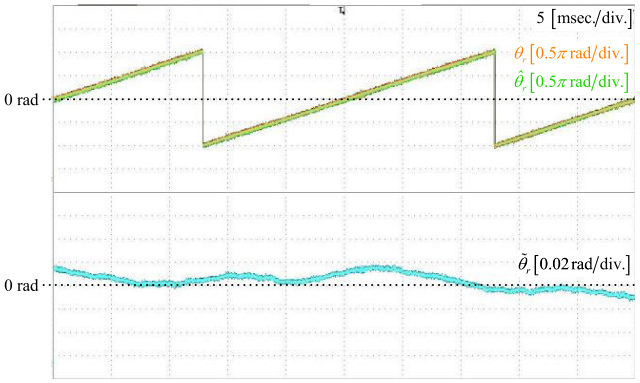

FIGURE 19. Experimental results: position estimation error of the proposed sensorelss method under 1,200 [r/min] rotor speed and 9 [Nm] load conditions. (a) real and estimated rotor position, and position error $\tilde{\theta}_r$.

Fig. 18 shows the estimated $\gamma\delta$-axis second parameters $\hat{p}_{\gamma\delta 2}$ by the RLS estimator under the rotor speed and the stator current variations. Initially, the estimated $\gamma\delta$-axis second parameters $\hat{p}_{\gamma\delta 2}$ are set to zero. From $t = 2$ [sec.], the parameters are estimated by the RLS estimator with high-frequency signals injection. From $t = 4$ to 4.5 [sec.], although it is not shown in the figure, the γ-axis current increases to 50% of the rated current to generate the γ-axis rotor flux, so the second parameter $\hat{p}_{\gamma 2}$ is decreased. From $t = 6$ [sec.], a step load of 9 [Nm] is applied. The δ-axis current increases, so the δ-axis second parameter $\hat{p}_{\delta 2}$ is decreased. From $t = 10$ to 16 [sec.], as the rotor speed increases to 1,200 [r/min.], the estimated $\gamma\delta$-axis second parameters $\hat{p}_{\gamma\delta 2}$ are significantly changed due to the back-EMF terms. This test results show that the $\gamma\delta$-axis second parameters $\hat{p}_{\gamma\delta 2}$ are estimated by the injected high-frequency signals even under the rotor speed variation conditions.

Fig. 19 shows the position estimation error of the proposed position-sensorless method under 1,200 [r/min.] rotor speed and 9 [Nm] load conditions. Fig. 19 shows the real and estimated rotor position, and position error $\tilde{\theta}_r$. In the proposed high-frequency signal injection sensorless method, the δ-axis square-pulse current is additionally

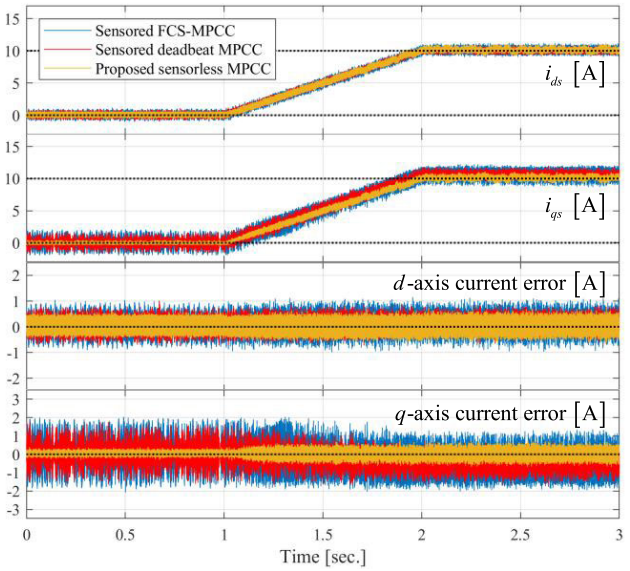

FIGURE 20. Experimental results: comparison of conventional FCS-MPCC [27], deadbeat MPCC [2], and the proposed MPCC with 100% dq-axis stator inductance errors under 1,200 [r/min] rotor speed.

injected for δ-axis parameters estimation unlike the conventional sensorless methods. The maximum position error $\tilde{\theta}_r$ is below –0.1 [rad.]. Experimental results confirm that the rotor position is estimated well although the square-pulse current is injected in the δ-axis.

Fig. 20 shows the comparison of the conventional methods and the proposed method. The blue line is the sensored FCS-MPCC [27], the red line is the sensored deadbeat MPCC [2], and the yellow line is the proposed position-sensorless MPCC. The tests are conducted with 100% dq-axis stator inductance errors (2. L_{ds} and 2. L_{qs}) at 1,200 [r/min] rotor speed. The rotor speed is controlled by the load motor (IM), and the test motor (SynRM) is in the current control mode. From $t = 1$ to 2 [sec.], the dq-axis current commands increase to 10 [A]. The ripple of dq-axis currents in the proposed method is smaller than that of other conventional MPCC methods. This is because the RLS estimator in the proposed method adjusts the stator inductance. The dq-axis current in the proposed method tracks well the command. But the current error in the conventional MPCC methods has a small offset component due to the inductance error.

Fig. 21 shows the phase current of the proposed MPCC under 1,200 [r/min] rotor speed and 9 [Nm] load conditions. Fig. 21(a) shows the a-phase current waveform, and Fig. 21(b) shows fast Fourier transform (FFT) results. In this test, the operating frequency is 40 [Hz], the frequency of the sinusoidal voltage injected in the γ-axis is 800 [Hz], the frequency of the square-pulse current injected in the δ-axis is 5,000 [Hz], and the switching frequency is 10,000 [Hz]. The total harmonic distortion (THD) of the a-phase current is 2.15%.

In addition, the computation time of the proposed algorithms in Fig. 10 is measured, which is listed in Table 2. The computation time for the RLS and the MPCC takes

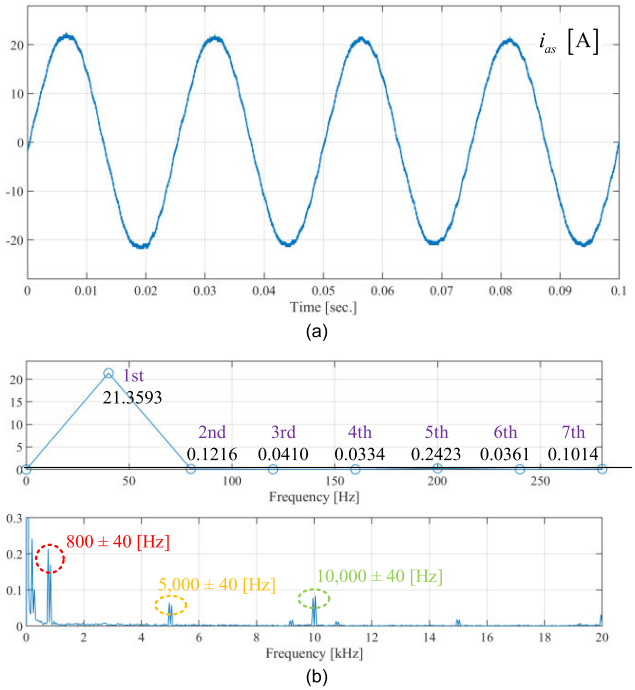

FIGURE 21. Experimental results: phase current of the proposed MPCC under 1,200 [r/min] rotor speed and 9 [Nm] load conditions. (a) a-phase current, (b) FFT results.

TABLE 2. Measured computation time of proposed algorithms.

Control block	Computation time [μsec.]
PI speed controller	2.35
Current control (MPCC)	8.77
Parameter estimation (RLS)	35.3
High-freq. sensorless	6.65

a relatively long time. It might not be easy to implement with a low-cost chip. But motor drives are used in various applications ranging from high to low-cost appliances. There are applications where the online parameter estimation and the position-sensorless control would outweigh the cost of implementation, justifying the increase in hardware cost.

VI. CONCLUSION

This paper proposes CCS-MPCC with the online parameter estimation for SynRMs controlled by high-frequency signals injection-based position-sensorless method. This method does not require accurate knowledge about the machine parameters and eliminates the need for the position sensor. The proposed method adopts the RLS algorithm for the online machine parameter estimation. Therefore, this method is robust to the parameter variations. In addition, this study proposes the modified high-frequency signal injection method, which injects the sinusoidal signal in the γ-axis to estimate the rotor position and the pulse signal in the δ-axis to estimate the machine parameters. The proposed sensorless method ensures stable operation at low-speed regions, including zero-speed. Simulation and experimental results are provided to validate the performance of the proposed method.

APPENDIX

The δ-axis current by the voltage command in (20) can be obtained with substituting (20) to (14) as:

$$\begin{aligned} &i_{\delta s}[k] \\ &= i_{\delta s}[k-1] + T_s p_{\delta 2}[k] \\ &\quad + T_s \left(\frac{i^*_{\delta sc}[k-2] - i^P_{\delta sc}[k-1] - T_s \hat{p}_{\delta 2l}[k-2]}{T_s \hat{p}_{\delta 1}[k-2]} \right) p_{\delta 1}[k] \end{aligned} \tag{27}$$

As previously mentioned in *section III*, the estimated parameters are considered as almost constant value during two switching periods. Therefore, the $[k-2]$th estimated parameters are set to $[k]$th values.

$$\begin{aligned} &i_{\delta s}[k] \\ &= i_{\delta s}[k-1] + T_s p_{\delta 2}[k] \\ &\quad + T_s \left(\frac{i^*_{\delta sc}[k-2] - i^P_{\delta sc}[k-1] - T_s \hat{p}_{\delta 2l}[k]}{T_s \hat{p}_{\delta 1}[k]} \right) p_{\delta 1}[k] \end{aligned} \tag{28}$$

If the estimated parameters by the RLS estimator are accurate, (28) is rewritten as:

$$i_{\delta s}[k] = i^*_{\delta sc}[k-2] + i_{\delta s}[k-1] - i^P_{\delta sc}[k-1] + T_s p_{\delta 2h}[k] \tag{29}$$

Substituting (18) to (29) yields the following.

$$\begin{aligned} i_{\delta s}[k] = i^*_{\delta sc}[k-2] + i_{\delta s}[k-1] + T_s p_{\delta 2h}[k] \\ - \left(\frac{\omega_i}{D+\omega_i} i_{\delta s}[k-2] + \Delta i^P_{\delta sc}[k-1] \right) \end{aligned} \tag{30}$$

The δ-axis current in (30) is rewritten by substituting (13) into (30) as:

$$\begin{aligned} i_{\delta s}[k] &= i^*_{\delta sc}[k-2] + (i_{\delta sc}[k-1] + i_{\delta sh}[k-1]) \\ &\quad + T_s p_{\delta 2h}[k] \\ &\quad - \frac{\omega_i}{D+\omega_i} (i_{\delta sc}[k-2] + i_{\delta sh}[k-2]) \\ &\quad - \Delta i^P_{\delta sc}[k-1] \\ &= i^*_{\delta sc}[k-2] + i_{\delta sh}[k-1] + T_s p_{\delta 2h}[k] \\ &\quad - \frac{\omega_i}{D+\omega_i} i_{\delta sh}[k-2] \\ &\quad + \left(i_{\delta sc}[k-1] - \Delta i^P_{\delta sc}[k-1] \right) \\ &\quad - \frac{\omega_i}{D+\omega_i} i_{\delta sc}[k-2] \end{aligned} \tag{31}$$

It is supposed that the predicted variation of the δ-axis current $\Delta i^P_{\delta sc}$ is accurate. Then, (31) is rewritten using (3) as:

$$\begin{aligned} i_{\delta s}[k] &\approx i^*_{\delta sc}[k-2] + i_{\delta sh}[k-1] + T_s p_{\delta 2h}[k] \\ &\quad - \frac{\omega_i}{D+\omega_i} i_{\delta sh}[k-2] \\ &\quad + i_{\delta sc}[k-2] - \frac{\omega_i}{D+\omega_i} i_{\delta sc}[k-2] \end{aligned} \tag{32}$$

Eq. (32) can be simplified as:

$$\begin{aligned} i_{\delta s}[k] &= i^*_{\delta sc}[k-2] + \underbrace{i_{\delta sh}[k-1] + T_s p_{\delta 2h}[k]}_{\text{high-frequency component}} \\ &+ \underbrace{\frac{-\omega_i}{D+\omega_i} i_{\delta sh}[k-2]}_{\text{filtered high-frequency component}} + \underbrace{\frac{D}{D+\omega_i} i_{\delta sc}[k-2]}_{\text{controller error}} \end{aligned} \tag{33}$$

REFERENCES

[1] B. Wang, X. Chen, Y. Yu, G. Wang, and D. Xu, "Robust predictive current control with online disturbance estimation for induction machine drives," *IEEE Trans. Power. Electron.*, vol. 32, no. 6, pp. 4663–4674, Jun. 2017.

[2] H.-T. Moon, H.-S. Kim, and M.-J. Youn, "A discrete-time predictive current control for PMSM," *IEEE Trans. Power Electron.*, vol. 18, no. 1, pp. 464–472, Jan. 2003.

[3] R. Mikail, I. Husain, Y. Sozer, M. S. Islam, and T. Sebastian, "A fixed switching frequency predictive current control method for switched reluctance machines," *IEEE Trans. Ind. Appl.*, vol. 50, no. 6, pp. 3717–3726, Nov./Dec. 2014.

[4] P. G. Carlet, F. Tinazzi, S. Bolognani, and M. Zigliotto, "An effective model-free predictive current control for synchronous reluctance motor drives," *IEEE Trans. Ind. Appl.*, vol. 55, no. 4, pp. 3781–3790, Jul./Aug. 2019.

[5] S. Vazquez, J. Rodriguez, M. Rivera, L. G. Franquelo, and M. Norambuena, "Model predictive control for power converters and drives: Advances and trends," *IEEE Trans. Ind. Electron.*, vol. 64, no. 2, pp. 935–947, Feb. 2017.

[6] B. Sneyers, D. W. Novotny, and T. A. Lipo, "Field weakening in buried permanent magnet AC motor drives," *IEEE Trans. Ind. Appl.*, vol. IA-21, no. 2, pp. 398–407, Mar./Apr. 1985.

[7] D. Reigosa, D. Fernandez, T. Tanimoto, T. Kato, and F. Briz, "Comparative analysis of BEMF and pulsating high-frequency current injection methods for PM temperature estimation in PMSMs," *IEEE Trans. Power Electron.*, vol. 32, no. 5, pp. 3691–3699, May 2017.

[8] C.-K. Lin, T.-H. Liu, J.-T. Yu, L.-C. Fu, and C.-F. Hsiao, "Model-free predictive current control for interior permanent-magnet synchronous motor drives based on current difference detection technique," *IEEE Trans. Ind. Electron.*, vol. 61, no. 2, pp. 667–681, Feb. 2014.

[9] F. Tinazzi, P. G. Carlet, S. Bolognani, and M. Zigliotto, "Motor parameter-free predictive current control of synchronous motors by recursive least-square self-commissioning model," *IEEE Trans. Ind. Electron.*, vol. 67, no. 11, pp. 9093–9100, Nov. 2020.

[10] M. Khalilzadeh, S. Vaez-Zadeh, and M. S. Eslahi, "Parameter-free predictive control of IPM motor drives with direct selection of optimum inverter voltage vectors," *IEEE J. Emerg. Sel. Topics Power Electron.*, vol. 9, no. 1, pp. 327–334, Feb. 2021.

[11] Y. Zhou, H. Li, and H. Zhang, "Model-free deadbeat predictive current control of a surface-mounted permanent magnet synchronous motor drive system," *J. Power Electron.*, vol. 18, no. 1, pp. 103–115, Jan. 2018.

[12] J.-H. Jang, S.-K. Sul, J.-I. Ha, K. Ide, and M. Sawamura, "Sensorless drive of surface-mounted permanent-magnet motor by high-frequency signal injection based on magnetic saliency," *IEEE Trans. Ind. Appl.*, vol. 39, no. 4, pp. 1031–1039, Jul. 2003.

[13] S. Kim, J.-I. Ha, and S.-K. Sul, "PWM switching frequency signal injection sensorless method in IPMSM," *IEEE Trans. Ind. Appl.*, vol. 48, no. 5, pp. 1576–1587, Sep./Oct. 2012.

[14] J.-I. Ha, S.-J. Kang, and S.-K. Sul, "Position-controlled synchronous reluctance motor without rotational transducer," *IEEE Trans. Ind. Appl.*, vol. 35, no. 6, pp. 1393–1398, Nov. 1999.

[15] Y. Inoue, K. Yamada, S. Morimoto, and M. Sanada, "Effectiveness of voltage error compensation and parameter identification for model-based sensorless control of IPMSM," *IEEE Trans. Ind. Appl.*, vol. 45, no. 1, pp. 213–221, Jan. 2009.

[16] M. Preindl and E. Schaltz, "Sensorless model predictive direct current control using novel second-order PLL observer for PMSM drive systems," *IEEE Trans. Ind. Electron.*, vol. 58, no. 9, pp. 4087–4095, Sep. 2012.

[17] L. Rovere, A. Formentini, A. Gaeta, P. Zanchetta, and M. Marchesoni, "Sensorless finite-control set model predictive control for IPMSM drives," *IEEE Trans. Ind. Electron.*, vol. 63, no. 9, pp. 5921–5931, Sep. 2016.

[18] M. S. Mubarok and T.-H. Liu, "Predictive controllers for dual-voltage vector current-slope sensorless IPMSM drives," *IEEE Access*, vol. 9, pp. 74855–74867, 2021.

[19] B. Nikmaram, S. A. Davari, P. Naderi, C. Garcia, and J. Rodriguez, "Sensorless simplified finite control set model predictive control of SynRM using finite position set algorithm," *IEEE Access*, vol. 9, pp. 47184–47193, 2021.

[20] X. Luo, A. Shen, Q. Tang, J. Liu, and J. Xu, "Two-step continuous-control set model predictive current control strategy for SPMSM sensorless drives," *IEEE Trans. Energy Convers.*, vol. 36, no. 2, pp. 1110–1120, Jun. 2021.

[21] H. S. Kim and K. Lee, "Parameter-free predictive current control for synchronous machine controlled by high-frequency signal injection sensorless," in *Proc. IEEE Energy Convers. Congr. Expo.*, Vancouver, BC, Canada, Oct. 2021, pp. 5036–5042.

[22] C.-E. Hwang, Y. Lee, and S.-K. Sul, "Analysis on position estimation error in position-sensorless operation of IPMSM using pulsating square wave signal injection," *IEEE Trans. Ind. Appl.*, vol. 55, no. 1, pp. 458–470, Jan. 2019.

[23] Y. Li, Z. Q. Zhu, D. Howe, C. M. Bingham, and D. A. Stone, "Improved rotor-position estimation by signal injection in brushless AC motors, accounting for cross-coupling magnetic saturation," *IEEE Trans. Ind. Appl.*, vol. 45, no. 5, pp. 1843–1850, Jul. 2009.

[24] S.-K. Chung, H.-S. Kim, C.-G. Kim, and M.-J. Youn, "A new instantaneous torque control of PM synchronous motor for high-performance direct-drive applications," *IEEE Trans. Power Electron.*, vol. 13, no. 3, pp. 388–400, May 1998.

[25] P. Cortes, J. Rodriguez, C. Silva, and A. Flores, "Delay compensation in model predictive current control of a three-phase inverter," *IEEE Trans. Ind. Electron.*, vol. 59, no. 2, pp. 1323–1325, Feb. 2012.

[26] S. Haykin, *Adaptive Filter Theory*. London, U.K.: Pearson, 1988, ch. 10.

[27] J. Rodriguez, H. Pontt, C. A. Silva, P. Correa, P. Lezana, P. Cortes, and U. Ammann, "Predictive current control of a voltage source inverter," *IEEE Trans. Ind. Electron.*, vol. 54, no. 1, pp. 495–503, Feb. 2007.

HYEON-SEONG KIM received the B.S. and M.S. degrees in mechatronics engineering from Incheon National University, Incheon, South Korea, in 2019 and 2021, respectively.

He is currently an Assistant Manager with the Electrical Equipment Research and Development Team, Dawonsys Company Ltd., Ansan, South Korea. His current research interests include motor drives for AC machines and power conversion systems.

KIBOK LEE (Member, IEEE) received the B.S. and M.S. degrees in electrical engineering from Korea University, Seoul, South Korea, in 2005 and 2007, respectively, and the Ph.D. degree in electrical engineering from North Carolina State University, Raleigh, NC, USA, in 2016.

From 2007 to 2011, he was a Research Engineer with the LG Electronics Research and Development Center, Seoul. From 2016 to 2018, he was a Senior Motor Control Engineer with the General Motors Powertrain Center, Pontiac, MI, USA. From 2018 to 2021, he was an Assistant Professor with Incheon National University, Incheon, South Korea. He is currently an Assistant Professor with the Department of Smart Mobility Engineering, Inha University, Incheon. His current research interests include motor drives, power conversion systems, and wireless power transfer systems.